An isogeometric analysis formulation for red blood cell electro-deformation modeling

Nicola A. Nodargi[a,b,*], Josef Kiendl[c], Paolo Bisegna[b], Federica Caselli[b], Laura De Lorenzis[a]

[a] *Institut für Angewandte Mechanik, Technische Universität Braunschweig, Pockelsstraße 3, 38106 Braunschweig, Germany*

[b] *Department of Civil Engineering and Computer Science, University of Rome "Tor Vergata", Via del Politecnico 1, 00133 Rome, Italy*

[c] *Department of Marine Technology, Norwegian University of Science and Technology, Otto Nielsens 10, 7052 Trondheim, Norway*

Abstract

An isogeometric analysis formulation for simulating red blood cell (RBC) electro-deformation is presented. Electrically-induced cell deformation experiments are receiving increasing attention as an attractive strategy for single-cell mechanical phenotyping. As the RBC structure consists in a very thin biological membrane enclosing a nearly-incompressible fluid, (i) a surface shell kinematic model and (ii) the imposition of the shell enclosed-volume conservation constraint are proposed within the isogeometric analysis framework. With regard to the electro-deformation, an accurate evaluation of the electric-field induced forces is achieved by the Maxwell stress tensor approach. A staggered fixed-point iteration scheme is then proposed for performing the electro-mechanical coupling, in order to use reliable mechanical and electrical problem solvers sequentially. Supported by the comparison with experimental results and reference solutions, numerical simulations concerning the large deformation of a RBC by optical tweezers and an *in silico* electro-deformation experiment prove the accuracy and the effectiveness of the proposed formulation.

Keywords: Isogeometric analysis, Thin shell, Biological membrane, Electro-deformation, Strong coupling

1. Introduction

Cell mechanical properties have been recognized by the biophysics community to be useful markers of cell state. In particular, the growing evidence that cell deformability may provide a label-free biomarker for determining e.g. metastatic potential, degree of differentiation, or cell activation [1], has prompted the development of a wide range of experimental techniques aiming at cell mechanical phenotyping (reviews can be found in [2, 3, 4]). Increasing

*Corresponding author

Email address: nodargi@ing.uniroma2.it (Nicola A. Nodargi)

attention has been recently devoted to electrically-induced cell deformation in microfluidic systems, which is especially attractive for being a potentially high-throughput technique. Among the cell types whose mechanical characterization has been explored through electro-deformation experiments [5, 6, 7, 8], a prominent position is taken by erythrocyte or red blood cell (RBC), due to the importance of its deformability in physiology and pathophysiology [9]. In fact erythrocyte deformability is crucial to microvascular function and becomes altered in various blood-related hereditary and non-hereditary diseases, such as malaria, sickle cell anemia, diabete mellitus, and cardiovascular disease [10]. As both the interpretation of experimental results and the identification of optimal experimental assay design call for aid from modeling and simulation strategies, the focus is here on the development of a computational approach to the RBC electro-deformation experiment.

From a structural standpoint, a RBC consists in a liquid capsule enclosed by a biological membrane, the latter being composed of a phospholipid bilayer and an underlying cytoskeleton, coupled to each other. The biological membrane behaves as a very thin shell (its thickness is less than 10 nm, while its diameter is about 8 μm), which derives its bending stiffness from the phospholipid bilayer and its membrane stiffness from the cytoskeleton. Additionally, the phospholipid bilayer enforces a local surface area conservation constraint. In turn, the nearly incompressible cytosol inside the biological membrane determines an enclosed-volume conservation constraint [11].

A standard approach to capture the mechanical behavior of biological membranes, often undergoing large rotations and deformations, is the use of Kirchhoff–Love shell finite element formulations [10, 12, 7]. Apart for the need of fine discretizations for an accurate description of the problem geometry, such a strategy suffers from computational issues related to the explicit use of nodal rotations as degrees of freedom in presence of the very small bending stiffness exhibited by biomembranes. A possible remedy within the context of the finite element method (FEM) relies on rotation-free shell formulations (see, e.g. [13]), not involving nodal rotations and approximating the element curvature on the basis of the transversal displacements of adjacent elements. Departing from shell models, alternative strategies are represented by the dissipative particle dynamics method [14, 15], whose application might be limited by computational demand, and element-free formulations, recently addressed in [16, 17, 18], although not considering the local surface area constraint nor the enclosed-volume conservation constraint. In the slightly different context of simulating the mechanical behavior of biological vesicles, i.e. biomembranes only exhibiting bending stiffness, also under the interaction with a surrounding medium, it is worth mentioning phase-field formulations [19, 20] and level-set methods [21, 22], which describe the vesicle in the fashion of a smeared interface. However, the extension of such approaches to account for the membrane stiffness does not appear completely straightforward. Moreover, their computational cost only appears justified by the flexibility of phase-field approaches in dealing with topological changes in the cell, which do not occur during RBC deformation.

Many of the drawbacks emerging from the above discussion are naturally overcome by isogeometric analysis (IGA), originally proposed in [23] as an extension of the standard FEM and typically adopting Non-Uniform Rational B-Splines (NURBS) as basis functions for both geometry and solution discretization. The most attractive advantages with respect

to standard FEM formulations for the present application are: (i) the ability to exactly describe complex geometries even at the coarsest level of refinement without requiring a meshing process, and (ii) the natural fulfillment of the C^1–continuity requirement of the spatial discretization to be used in the Kirchhoff–Love shell model. Several Kirchhoff–Love shell isogeometric formulations have been proposed to date (for instance, see [24, 25]), and their applications to biological membranes have been considered as well [26]. Yet, compared to biological membranes, the description of the RBC mechanical behavior further requires the imposition of local surface area and enclosed-volume conservation constraints.

With respect to the electro-mechanical coupling, the attractive ability of IGA to accurately represent smooth exact geometries with a relatively low number of degrees of freedom and avoiding typical issues of FEM such as mesh distortion during simulations (as suggested from the application of IGA to the analogous multi-physics problem of fluid-structure interaction [27, 28]), does not seem to have been exploited so far. In particular, the coupling might benefit from an accurate estimate of the mechanical forces induced by the electric field.

Aim of the present work is to develop a robust IGA formulation for simulating RBC electro-deformation. The RBC biological membrane is modeled resorting to a surface shell formulation which is similar to the Kirchhoff–Love shell formulation discussed in [25]. A homogenized microstructurally-based constitutive law, based on the (first-order) Cauchy–Born rule [29], is adopted for the membrane behavior (generalized Cauchy-Born rules, as discussed in [30, 31, 32, 33], might be alternatively considered, although computationally more demanding [16]). Local surface area conservation constraint is here explicitly involved. Thanks to such a multiscale framework, on the one hand the specific mechanical nature of the biomembrane principal constituents is accurately accounted for, on the other hand the computational efficiency of a continuum approach is enjoyed [11, 34, 15, 16]. The Helfrich model is assumed for the bending behavior [35]. The RBC mechanical description is completed by the enclosed-volume conservation constraint, which is enforced through a penalty method at structural level. In order to determine the electric field distribution in the domain of the electro-deformation experiment, conforming parametrizations of intracellular space, biological membrane and suspending fluid are considered. The mechanical forces induced by the electric field acting upon the RBC are evaluated adopting the Maxwell stress tensor approach [36, 7, 8]. A staggered fixed-point iteration scheme is then applied to implement the electro-mechanical (strong) coupling. Consequently, electrical and mechanical problems are solved sequentially. The electrical problem consists in the computation of the mechanical forces induced by the electric field for a prescribed geometry of the RBC, whereas the mechanical problem consists in the computation of the RBC configuration in equilibrium for prescribed load.

Numerical simulations are reported for assessing accuracy, robustness and effectiveness of the proposed isogeometric formulation. A purely mechanical application consists in reproducing experiments of RBC large deformation by optical tweezers available in the literature [34]. An *in silico* RBC electro-deformation experiment is then discussed. From the comparison of numerical results with experimental evidences and reference solutions, the capabilities and potentialities of the present formulation, along with a reduction in computational cost

compared to the FEM alternative, are highlighted.

The present paper is organized as follows. In Section 2 the mechanical problem is discussed, dealing with the surface shell kinematic model, the RBC constitutive law, the variational formulation of the equilibrium problem and its isogeometric discretization. In Section 3 the electrical problem of RBC immersed in a suspending fluid and subjected to an applied electrical field is presented, including the derivation of the mechanical loads induced by the electric field acting over the cell. In Section 4 the proposed staggered fixed-point scheme for performing the electro-mechanical coupling is described. Numerical simulations are reported in Section 5 and conclusions are outlined in Section 6. Finally, details on the mechanical problem linearization are given in Appendix A.

2. Mechanical problem

The structure of a RBC consists in a liquid capsule enclosed by a biological membrane. The biological membrane can be modeled as a shell surface, exhibiting both membrane and bending stiffnesses. Because of the near-incompressibility of the inner liquid (cytosol), such shell surface is subjected to an enclosed-volume conservation constraint. In this section, after presenting the shell surface kinematic model, a variational formulation of the RBC mechanical evolution problem is presented. Moreover, its isogeometric discretization is discussed.

In the following, unless otherwise stated, greek and latin indices take respectively values in $\{1,2\}$ and $\{1,2,3\}$, and Einstein summation convention is used.

2.1. Kinematic model

Let the shell reference surface Γ be parametrized by a map $\boldsymbol{X} \in H^2(\hat{\Omega})^3$, where $\hat{\Omega} \subset \mathbb{R}^2$ is a domain representing the parameter set and H^2 denotes the space of square integrable functions along with their first and second weak derivatives. It is assumed that the two vectors:

$$\boldsymbol{G}_\alpha(\boldsymbol{\xi}) = \boldsymbol{X}_{,\alpha}(\boldsymbol{\xi})\,, \tag{1}$$

in which the notation $(\cdot)_{,\alpha}$ is introduced for the partial derivative with respect to the parameter coordinate ξ_α, are linearly independent at a.e. point $\boldsymbol{\xi} \in \hat{\Omega}$. Accordingly, these two vectors span the tangent plane to Γ at $\boldsymbol{X}(\boldsymbol{\xi})$ and it is possible to consider the director to Γ at $\boldsymbol{X}(\boldsymbol{\xi})$, i.e. the unit normal vector, as given by:

$$\boldsymbol{G}_3(\boldsymbol{\xi}) = \frac{\tilde{\boldsymbol{G}}_3(\boldsymbol{\xi})}{A(\boldsymbol{\xi})}, \quad \tilde{\boldsymbol{G}}_3(\boldsymbol{\xi}) = \boldsymbol{G}_1(\boldsymbol{\xi}) \times \boldsymbol{G}_2(\boldsymbol{\xi})\,, \quad A(\boldsymbol{\xi}) = \|\tilde{\boldsymbol{G}}_3(\boldsymbol{\xi})\|, \tag{2}$$

where $\times$ denotes cross product and $\tilde{\boldsymbol{G}}_3(\boldsymbol{\xi})$ and $A(\boldsymbol{\xi})$ are respectively referred to as the normal vector and the area element at $\boldsymbol{X}(\boldsymbol{\xi})$. The three vectors $\boldsymbol{G}_i(\boldsymbol{\xi})$ constitute the covariant basis at point $\boldsymbol{X}(\boldsymbol{\xi})$, whereas the three vectors defined by the relationships:

$$\boldsymbol{G}^i(\boldsymbol{\xi}) \cdot \boldsymbol{G}_j(\boldsymbol{\xi}) = \delta^i_j, \tag{3}$$

with $\cdot$ denoting scalar product and δ^i_j denoting the Kronecker symbol, constitute the contravariant basis at point $\boldsymbol{X}(\boldsymbol{\xi})$ (for instance, see [37]).

Within the present kinematic model, a displacement field $\boldsymbol{u} \in H^2(\hat{\Omega})^3$, mapping the shell reference surface Γ onto the shell current surface γ, is considered. Accordingly, γ is parametrized by a map $\boldsymbol{x} \in H^2(\hat{\Omega})^3$, given by:

$$\boldsymbol{x}(\boldsymbol{\xi}) = \boldsymbol{X}(\boldsymbol{\xi}) + \boldsymbol{u}(\boldsymbol{\xi}) \,, \tag{4}$$

with $\boldsymbol{u}$ as the surface displacement field. It is required that the two vectors $\boldsymbol{g}_\alpha(\boldsymbol{\xi}) = \boldsymbol{x}_{,\alpha}(\boldsymbol{\xi})$ are linearly independent at a.e. point $\boldsymbol{\xi} \in \hat{\Omega}$. Equations analogous to (1), (2) and (3) yield the covariant basis $\boldsymbol{g}_i(\boldsymbol{\xi})$, the contravariant basis $\boldsymbol{g}^i(\boldsymbol{\xi})$ and the area element $a(\boldsymbol{\xi})$ at point $\boldsymbol{x}(\boldsymbol{\xi})$.

The surface deformation is completely described in terms of the Green-Lagrange strain tensor, i.e. the change of metric tensor :

$$\boldsymbol{\varepsilon}(\boldsymbol{\xi}) = \frac{1}{2} \left[\boldsymbol{g}_\alpha(\boldsymbol{\xi}) \cdot \boldsymbol{g}_\beta(\boldsymbol{\xi}) - \boldsymbol{G}_\alpha(\boldsymbol{\xi}) \cdot \boldsymbol{G}_\beta(\boldsymbol{\xi}) \right] \boldsymbol{G}^\alpha(\boldsymbol{\xi}) \otimes \boldsymbol{G}^\beta(\boldsymbol{\xi}) \,, \tag{5}$$

and of the change of curvature tensor:

$$\boldsymbol{\chi}(\boldsymbol{\xi}) = - \left[\boldsymbol{g}_{\alpha,\beta}(\boldsymbol{\xi}) \cdot \boldsymbol{g}_3(\boldsymbol{\xi}) - \boldsymbol{G}_{\alpha,\beta}(\boldsymbol{\xi}) \cdot \boldsymbol{G}_3(\boldsymbol{\xi}) \right] \boldsymbol{G}^\alpha(\boldsymbol{\xi}) \otimes \boldsymbol{G}^\beta(\boldsymbol{\xi}) \,, \tag{6}$$

where $\otimes$ denotes tensor product (e.g., see [38]). In particular, the stretch $\lambda_{\boldsymbol{e}}(\boldsymbol{\xi})$ along a prescribed unit vector $\boldsymbol{e}$ lying in the shell surface tangent plane and the areal stretch $\Lambda(\boldsymbol{\xi})$ are:

$$\lambda_{\boldsymbol{e}}(\boldsymbol{\xi}) = \sqrt{1 + 2\boldsymbol{\varepsilon}(\boldsymbol{\xi})\, \boldsymbol{e} \cdot \boldsymbol{e}}, \quad \Lambda(\boldsymbol{\xi}) = a(\boldsymbol{\xi}) \,/ A(\boldsymbol{\xi}) \,. \tag{7}$$

The following developments also require the computation of the volume enclosed by the shell in reference configuration V and in current configuration v. Applying the divergence theorem, they result to be:

$$V = \frac{1}{3} \int_\Gamma \boldsymbol{X} \cdot \boldsymbol{G}_3 \, \mathrm{d}\Gamma, \quad v = \frac{1}{3} \int_\Gamma \boldsymbol{x} \cdot \boldsymbol{g}_3 \, \Lambda \, \mathrm{d}\Gamma, \tag{8}$$

whence the change of enclosed volume is $v - V$.

For the variational formulation to be discussed in Section 2.3, the variation of the change of metric tensor $\delta\boldsymbol{\varepsilon}$, of the change of curvature tensor $\delta\boldsymbol{\chi}$ and of the change of enclosed volume δv with respect to a variation of the displacement field $\delta\boldsymbol{u}$ needs to be computed. As a preliminary step, on observing that the reference surface configuration $\boldsymbol{X}$ does not depend on the displacement field $\boldsymbol{u}$, the variation of the current surface configuration $\boldsymbol{x}$ is investigated. In particular, equations (4), (1) and (2) yield:

$$\delta\boldsymbol{x}(\boldsymbol{\xi}) = \delta\boldsymbol{u}(\boldsymbol{\xi}) \,, \quad \delta\boldsymbol{g}_\alpha(\boldsymbol{\xi}) = \delta\boldsymbol{u}_{,\alpha}(\boldsymbol{\xi}) \,, \quad \delta\boldsymbol{g}_3(\boldsymbol{\xi}) = \left[\boldsymbol{I} - \boldsymbol{g}_3(\boldsymbol{\xi}) \otimes \boldsymbol{g}_3(\boldsymbol{\xi}) \right] \frac{\delta\tilde{\boldsymbol{g}}_3(\boldsymbol{\xi})}{a(\boldsymbol{\xi})}, \tag{9}$$

where $\boldsymbol{I}$ denotes the identity tensor and the following relationships hold true:

$$\delta\tilde{\boldsymbol{g}}_3(\boldsymbol{\xi}) = \delta\boldsymbol{g}_1(\boldsymbol{\xi}) \times \boldsymbol{g}_2(\boldsymbol{\xi}) + \boldsymbol{g}_1(\boldsymbol{\xi}) \times \delta\boldsymbol{g}_2(\boldsymbol{\xi}) \,, \quad \delta a(\boldsymbol{\xi}) = \boldsymbol{g}_3(\boldsymbol{\xi}) \cdot \delta\tilde{\boldsymbol{g}}_3(\boldsymbol{\xi}) \,. \tag{10}$$

Consequently, equations (5) and (6) give:

$$\delta\boldsymbol{\varepsilon}(\boldsymbol{\xi}) = \frac{1}{2}\left[\delta\boldsymbol{g}_\alpha(\boldsymbol{\xi})\cdot\boldsymbol{g}_\beta(\boldsymbol{\xi}) + \boldsymbol{g}_\alpha(\boldsymbol{\xi})\cdot\delta\boldsymbol{g}_\beta(\boldsymbol{\xi})\right]\boldsymbol{G}^\alpha(\boldsymbol{\xi})\otimes\boldsymbol{G}^\beta(\boldsymbol{\xi})\,, \tag{11}$$

$$\delta\boldsymbol{\chi}(\boldsymbol{\xi}) = -\left[\delta\boldsymbol{g}_{\alpha,\beta}(\boldsymbol{\xi})\cdot\boldsymbol{g}_3(\boldsymbol{\xi}) + \boldsymbol{g}_{\alpha,\beta}(\boldsymbol{\xi})\cdot\delta\boldsymbol{g}_3(\boldsymbol{\xi})\right]\boldsymbol{G}^\alpha(\boldsymbol{\xi})\otimes\boldsymbol{G}^\beta(\boldsymbol{\xi})\,, \tag{12}$$

whereas from equations (8):

$$\delta v = \frac{1}{3}\int_\Gamma \left[\delta\boldsymbol{x}\cdot\boldsymbol{g}_3\,\Lambda + \boldsymbol{x}\cdot(\delta\boldsymbol{g}_3\,\Lambda + \boldsymbol{g}_3\,\delta\Lambda)\right]\,\mathrm{d}\Gamma, \tag{13}$$

in which, from equation $(7)_2$:

$$\delta\Lambda(\boldsymbol{\xi}) = \delta a(\boldsymbol{\xi})\,/A(\boldsymbol{\xi})\,. \tag{14}$$

2.2. Constitutive model

For an accurate constitutive modeling of a RBC, the contribution of its constituents, i.e. biological membrane and cytosol, has to be accounted for. As schematically depicted in Figure 1(a), the biological membrane itself is a composite structure, composed of a phospholipid bilayer and an underlying spectrin network (cytoskeleton), coupled to each other by integral membrane proteins. The biological membrane exhibits both membrane and bending stiffnesses, whereas the cytosol is responsible of an enclosed-volume conservation constraint. Accordingly, the following internal free energy potential, similar to the one adopted in [13], is considered:

$$\mathcal{W}_{\mathrm{int}} = \mathcal{W}_{\mathrm{m}} + \mathcal{W}_{\mathrm{b}} + \mathcal{W}_{\mathrm{v}}, \tag{15}$$

where $\mathcal{W}_{\mathrm{m}}$ is the shell membrane contribution, $\mathcal{W}_{\mathrm{b}}$ is the shell bending contribution and $\mathcal{W}_{\mathrm{v}}$ is the volume contribution. In this section, each energy contribution is discussed in detail.

2.2.1. Membrane behavior

The membrane stiffness of the biological membrane arises from the spectrin network structure. Following the approach discussed in [39, 40, 11, 41], the spectrin network is modeled as a regular triangular network (Figure 1(b)), whose constituents are actin junction complexes (vertices), spectrin links (sides) and triangular plaquettes attached to phospholipid bilayer (triangles).

In order to determine the homogenized membrane energy of the biological membrane, a single equilateral triangle is considered as Repetitive Unit Cell. Let $\psi = \{0, 2\pi/3, 4\pi/3\}$ denote the polar angles along which the spectrin links lie and $\boldsymbol{e}(\psi)$ the relevant directions (Figure 1(c)). Upon neglecting fluctuations due to local inhomogeneities, the triangle undergoes an in-plane (uniform) strain described by the macroscopic Green-Lagrange strain tensor $\boldsymbol{\varepsilon}$. According to the worm-like chain model [42, 43, 13], the free energy stored in each spectrin link turns out to be:

$$w_{\mathrm{sl}}(\psi) = \frac{k_{\mathrm{B}}TL_0^2}{4pL_{\max}}\frac{\left[3L_{\max} - 2\lambda_{\boldsymbol{e}}(\psi)L_0\right]\lambda_{\boldsymbol{e}}(\psi)^2}{L_{\max} - \lambda_{\boldsymbol{e}}(\psi)L_0}\,, \quad \lambda_{\boldsymbol{e}}(\psi) < \frac{L_{\max}}{L_0}, \tag{16}$$

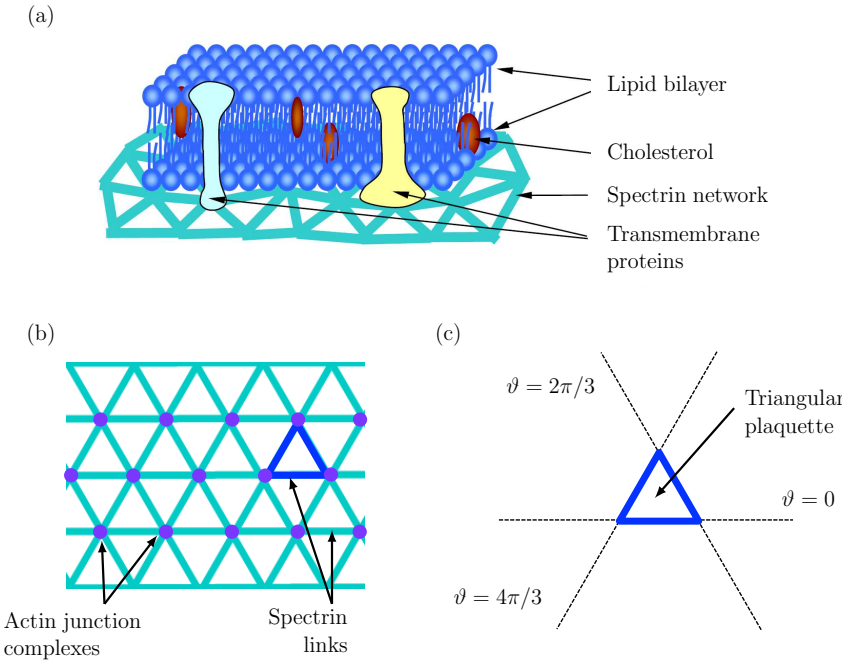

Figure 1: RBC biological membrane: (a) schematic illustration of biomembrane constituents (not to scale), (b) regular triangular network model and (c) relevant repetitive unit cell, reprinted with permission from [13].

where k_{B} is the Boltzmann constant, T is the absolute temperature, p is the persistence length, $L_{\max}$ is the contour chain maximum length and L_0 is the undeformed network chain length. It is remarked that the free energy w_{sl} blows up to infinity as the spectrin link stretch $\lambda_{\boldsymbol{e}}$ approaches unity. As a consequence, condition $(16)_2$ requires the current network chain length $\lambda_{\boldsymbol{e}}(\psi)L_0$ to be bounded by the contour chain maximum length $L_{\max}$. By equation $(7)_1$, that amounts at the imposition of a constraint on the Green-Lagrange strain tensor $\boldsymbol{\varepsilon}$. On the other hand, the free energy stored in the triangular plaquette can be estimated as [11]:

$$w_{\mathrm{tp}} = \frac{C_{\mathrm{q}}}{(\Lambda A_{\mathrm{tp}})^q}, \tag{17}$$

where $A_{\mathrm{tp}} = L_0^2\sqrt{3}/4$ is the network triangular plaquette reference area, q is a suitable exponent and the constant C_{q} is determined by imposing that the triangular network is stress-free for a vanishing applied Green-Lagrange strain tensor $\boldsymbol{\varepsilon}$:

$$C_{\mathrm{q}} = \frac{3}{16}\frac{k_{\mathrm{B}}T A_{\mathrm{tp}}^q L_{\max}}{pq}\frac{(6 - 9x_0 + 4x_0^2)}{(1 - x_0)^2}, \quad x_0 = \frac{L_0}{L_{\max}}. \tag{18}$$

Due to the conservation of the total number of lipid molecules over the biomembrane, surface area modifications are locally prevented. Such constraint is accounted for by considering an additional energy term [11]:

$$w_{\mathrm{s}} = \frac{1}{2}\, k_{\mathrm{s}}\, A_{\mathrm{tp}}\, (\Lambda - 1)^2\,, \tag{19}$$

in which k_s is a suitable penalty parameter.

Finally, according to the Cauchy–Born rule [29], the membrane free energy density w_m (homogenized with respect to the shell reference surface area) and the corresponding membrane free energy $\mathcal{W}_\mathrm{m}$ result to be:

$$w_\mathrm{m} = \frac{1}{A_\mathrm{tp}} \left[\sum_\psi w_\mathrm{sl}(\psi) + w_\mathrm{tp} + w_\mathrm{s} \right], \quad \mathcal{W}_\mathrm{m} = \int_\Gamma w_\mathrm{m} \, \mathrm{d}\Gamma. \tag{20}$$

The shell membrane forces (acting on an area element in the reference configuration) are finally introduced by:

$$\boldsymbol{n} = \frac{\partial w_\mathrm{m}}{\partial \boldsymbol{\varepsilon}}. \tag{21}$$

2.2.2. Bending behavior

The bending stiffness of the biological membrane arises from the phospholipid bilayer. Adopting the Helfrich model [35], the bending free energy density w_b (with respect to the shell current surface area) and the corresponding bending free energy $\mathcal{W}_\mathrm{b}$ can be evaluated as:

$$w_\mathrm{b} = \frac{k_\mathrm{c}}{2} J^2 + k_\mathrm{g} K, \quad \mathcal{W}_\mathrm{b} = \int_\Gamma w_\mathrm{b} \, \Lambda \, \mathrm{d}\Gamma, \tag{22}$$

where, denoting by tr and det the trace and determinant operators respectively, $J = \mathrm{tr}\, \boldsymbol{\chi}$ is the change of total curvature and $K = \det \boldsymbol{\chi}$ is related to the change of Gaussian curvature. Accordingly, the shell bending forces (acting on an area element in the current configuration) are given by:

$$\boldsymbol{m} = \frac{\partial w_\mathrm{b}}{\partial \boldsymbol{\chi}}. \tag{23}$$

2.2.3. Enclosed-volume conservation constraint

The RBC enclosed-volume conservation constraint arises from the near-incompressibility of the cytosol. Resorting to the penalty method, the volume energy contribution is [11]:

$$\mathcal{W}_\mathrm{v} = \frac{1}{2} \frac{k_\mathrm{v}}{V} \left(v - V \right)^2, \tag{24}$$

where k_v is a suitable penalty parameter and V [resp., v] has been introduced in equation (8) for the volume enclosed by the shell in reference [resp., current] configuration. The following definition is finally considered:

$$p = \frac{\partial \mathcal{W}_\mathrm{v}}{\partial v}, \tag{25}$$

with the meaning of shell inner pressure.

2.3. Variational formulation

A standard displacement-based variational formulation for the mechanical evolution of the RBC is considered. Consequently, the structural equilibrium condition is derived by imposing the stationarity of the total energy:

$$\mathcal{W} = \mathcal{W}_\mathrm{int} - \mathcal{W}_\mathrm{ext}, \tag{26}$$

where $\mathcal{W}_{\text{int}}$ is the internal free energy defined in Section 2.2 and $\mathcal{W}_{\text{ext}}$ is the potential of external loads, with respect to any variation of the displacement field $\delta\boldsymbol{u}$:

$$0 = \delta\mathcal{W} = \delta\mathcal{W}_{\text{int}} - \delta\mathcal{W}_{\text{ext}}. \tag{27}$$

In particular, the variation of the internal free energy $\delta\mathcal{W}_{\text{int}}$ is derived from equations (20), (22) and (24):

$$\delta\mathcal{W}_{\text{int}} = \int_\Gamma \boldsymbol{n} : \delta\boldsymbol{\varepsilon}\, \mathrm{d}\Gamma + \int_\Gamma \left(\boldsymbol{m} : \delta\boldsymbol{\chi}\, \Lambda + w_{\text{b}}\, \delta\Lambda\right)\, \mathrm{d}\Gamma + p\, \delta v, \tag{28}$$

where : denotes tensor contraction, the variations of the change of metric tensor $\delta\boldsymbol{\varepsilon}$, of the change of curvature tensor $\delta\boldsymbol{\chi}$ and of the change of enclosed volume δv are given in equations (11)–(13), respectively, and the shell membrane forces $\boldsymbol{n}$, the shell bending forces $\boldsymbol{m}$ and the shell inner pressure p are introduced in equations (21), (23) and (25), respectively.

2.4. Isogeometric discretization

Basic idea of IGA is to assume basis functions used in CAD (typically NURBS) for approximating both geometry and solution. Accordingly, the reference surface parametrization and the surface displacement are expressed by:

$$\boldsymbol{X}(\boldsymbol{\xi}) = R_I(\boldsymbol{\xi})\, \hat{\boldsymbol{X}}_I, \quad \boldsymbol{u}(\boldsymbol{\xi}) = R_I(\boldsymbol{\xi})\, \hat{\boldsymbol{u}}_I, \tag{29}$$

where R_I is the basis function associated to the control point I (e.g. see [44]), and $\hat{\boldsymbol{X}}_I$ and $\hat{\boldsymbol{u}}_I$ denote its reference coordinate and displacement, respectively. Correspondingly, the current surface parametrization results to be:

$$\boldsymbol{x}(\boldsymbol{\xi}) = R_I(\boldsymbol{\xi}) \left(\hat{\boldsymbol{X}}_I + \hat{\boldsymbol{u}}_I\right). \tag{30}$$

It is noted that the parametric coordinates $\boldsymbol{\xi}$ are here identified with the isogeometric natural coordinates and the parameter space $\hat{\Omega}$ descends from suitable knot vectors. Henceforth, the dependence on $\boldsymbol{\xi}$ will be omitted whenever no confusion may arise.
From reference and current surface discretizations, respectively in (29) and (30), the relevant discretized covariant bases can be derived. In particular, the tangent planes are spanned by:

$$\boldsymbol{G}_\alpha = R_{I,\alpha} \hat{\boldsymbol{X}}_I, \quad \boldsymbol{g}_\alpha = R_{I,\alpha} \left(\hat{\boldsymbol{X}}_I + \hat{\boldsymbol{u}}_I\right), \tag{31}$$

whence discretized normal vectors, area elements and directors can be computed for both reference and current surface using equations (2). As a consequence, the discretizations of the change of metric tensor $\boldsymbol{\varepsilon}$, of the change of curvature tensor $\boldsymbol{\chi}$ and of the change of enclosed volume $v - V$ follow from equations (5), (6) and (8), respectively.
Analogously, the discretized variations of the current surface configuration are derived from equations $(9)_{1\text{–}2}$:

$$\delta\boldsymbol{x} = R_I\, \delta\hat{\boldsymbol{u}}_I, \quad \delta\boldsymbol{g}_\alpha = R_{I,\alpha}\, \delta\hat{\boldsymbol{u}}_I, \tag{32}$$

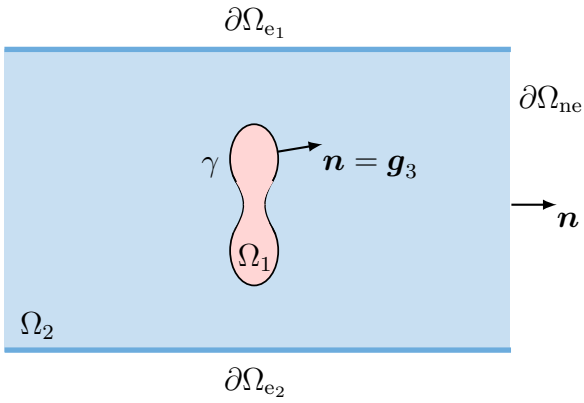

Figure 2: Electrical problem.

and the discretized variations of the change of metric tensor $\delta\boldsymbol{\varepsilon}$, of the change of curvature tensor $\delta\boldsymbol{\chi}$ and of the change of enclosed volume δv follow from equations (9)–(14).

The structural equilibrium condition (27) can be finally put in a customary residual form:

$$\mathbf{0} = \boldsymbol{r} = \boldsymbol{q}_{\text{ext}} - \boldsymbol{q}_{\text{int}}, \tag{33}$$

where the control point internal and external forces, $\boldsymbol{q}_{\text{int}}$ and $\boldsymbol{q}_{\text{ext}}$ respectively, are defined by:

$$\boldsymbol{q}_{\text{int}} \cdot \delta\hat{\boldsymbol{u}} = \delta\mathcal{W}_{\text{int}}, \quad \boldsymbol{q}_{\text{ext}} \cdot \delta\hat{\boldsymbol{u}} = \delta\mathcal{W}_{\text{ext}}. \tag{34}$$

Here, the discretized variation of the internal free energy $\delta\mathcal{W}_{\text{int}}$ follows from equation (28). It is also remarked that the control point external forces $\boldsymbol{q}_{\text{ext}}$ relevant to the electro-deformation problem have to be derived from the forces induced by the electric field (Section 3).
In Appendix A the linearization of the structural equilibrium equations (33) with respect to the control point displacements $\hat{\boldsymbol{u}}$, needed e.g. for adopting Newton's method of solution, is performed.

3. Electrical problem

In this section, the electrical problem of a RBC inside a suspending fluid, subjected to an applied electric field, is considered. Attention is also devoted to the derivation of the forces induced by the electric field over the erythrocyte. Finally, some details concerning the isogeometric formulation are discussed.

3.1. Governing equations and weak formulation

As depicted in Figure 2, the electrical problem domain consists in the union of two homogeneous conductive regions Ω_1 and Ω_2, respectively modeling the intracellular space and a suspending fluid. Each region is characterized by relative permittivity ε_k and conductivity σ_k, with $k = 1, 2$. The biological membrane γ separating the intracellular space from the suspending fluid is modeled as a two-dimensional interface, with conductance G and

capacitance C per unit area. The boundary of the domain is divided into an insulating part $\partial\Omega_{\mathrm{ne}}$, and a part covered by electrodes $\partial\Omega_{\mathrm{e}}$, which generate the electric field and are characterized by conductance G_{e} and capacitance C_{e} per unit area.

Under the quasistatic approximation, let φ denote the electric potential, from which the electric field can be derived as $\boldsymbol{e} = -\nabla\varphi$, with ∇ as the spatial gradient operator. In the following, time-harmonic fields are considered. Accordingly, let Φ denote the phasor of the electric potential $\varphi = \Re\left(\Phi e^{\mathrm{i}\omega t}\right)$, where i is the imaginary unit, ω is the circular frequency and $\Re$ is the real part operator. The electrical problem can be then stated in the Fourier domain. In particular, the electric conduction in the whole domain is governed by the divergence of the Maxwell–Ampère law:

$$-\operatorname{div}\left(\sigma^*\nabla\Phi\right) = 0 \quad \text{in } \Omega_1 \cup \Omega_2, \tag{35}$$

where div denotes the spatial divergence operator and $\sigma^* = \sigma_k + \mathrm{i}\varepsilon_k\varepsilon_0$ is the complex conductivity of the region Ω_k, with ε_0 as the vacuum permittivity. The continuity of the current flux density through the interface and the interface admittance behavior are respectively accounted for by the conditions:

$$\begin{aligned} 0 &= \left[\!\left[\sigma^*\nabla\Phi\cdot\boldsymbol{n}\right]\!\right] \quad \text{on } \gamma, \\ Y\left[\!\left[\Phi\right]\!\right] &= \sigma^*\nabla\Phi\cdot\boldsymbol{n} \qquad \text{on } \gamma, \end{aligned} \tag{36}$$

in which $[\![\cdot]\!]$ denotes the jump operator across the interface, $Y = G + \mathrm{i}\omega C$ is the interface admittance per unit area and $\boldsymbol{n}$ is the interface outward normal, coinciding with the basis vector $\boldsymbol{g}_3$ in the notation of Section 2. Finally, the insulating (natural) boundary condition on $\partial\Omega_{\mathrm{ne}}$ results to be:

$$\sigma^*\nabla\Phi\cdot\boldsymbol{n} = 0 \quad \text{on } \partial\Omega_{\mathrm{ne}}, \tag{37}$$

whereas the (Robin) boundary condition for the i-th electrode is [45]:

$$Y_{\mathrm{e}}\left(\Phi_i - \Phi\right) = \sigma^*\nabla\Phi\cdot\boldsymbol{n} \quad \text{on } \partial\Omega_{\mathrm{e}_i}, \tag{38}$$

with $Y_{\mathrm{e}} = G_{\mathrm{e}} + \mathrm{i}\omega C_{\mathrm{e}}$ as the electrode admittance per unit area and Φ_i as the phasor of the electrode potential $\varphi_i = \Re\left(\Phi_i e^{\mathrm{i}\omega t}\right)$. In both equations (37) and (38), $\boldsymbol{n}$ denotes the outward normal to the domain boundary.

As starting point for an isogeometric discretization of the electrical problem (35)–(38), its weak formulation is derived in the following form:

$$\int_{\Omega_1\cup\Omega_2} \sigma^*\nabla\Phi\cdot\nabla\overline{\delta\Phi}\,\mathrm{d}\Omega + \int_\gamma Y\left[\!\left[\Phi\right]\!\right]\left[\!\left[\,\overline{\delta\Phi}\,\right]\!\right]\,\mathrm{d}\gamma + \sum_i \int_{\partial\Omega_{\mathrm{e}_i}} Y_{\mathrm{e}}\Phi\,\overline{\delta\Phi}\,\mathrm{d}S = \sum_i \int_{\partial\Omega_{\mathrm{e}_i}} Y_{\mathrm{e}}\Phi_i\,\overline{\delta\Phi}\,\mathrm{d}S, \tag{39}$$

where $\delta\Phi$ is an arbitrary variation of the electric potential phasor Φ and the overline denotes complex conjugation. As discussed in Section 3.3, once the electric potential phasor Φ is computed, the electric field phasor $\boldsymbol{E}$ can be derived:

$$\boldsymbol{E} = -\nabla\Phi, \tag{40}$$

whence the electric field follows by $\boldsymbol{e} = \Re\left(\boldsymbol{E}e^{\mathrm{i}\omega t}\right)$.

3.2. Mechanical loads induced by the electric field

Following the variational approach discussed in [36, 46], the mechanical loads induced by the electric field can be derived by computing the variation of the electric field energy with respect to a variation of the configuration. The electric field energy corresponding to the formulation in Section 3.1 results to be:

$$\mathcal{W}_{\mathrm{el}} = \int_{\Omega_1 \cup \Omega_2} \frac{1}{2}\, \varepsilon\, |\boldsymbol{e}|^2 \,\mathrm{d}\Omega + \int_{\gamma} \frac{1}{2}\, C [\![\varphi]\!]^2 \,\mathrm{d}\gamma + \sum_i \int_{\partial\Omega_{\mathrm{e}_i}} \frac{1}{2}\, C_{\mathrm{e}}\, (\varphi - \varphi_i)^2 \,\mathrm{d}S, \tag{41}$$

in which $|\cdot|$ denotes the vector euclidean norm. By resorting to the notion of configurational derivative, the variation of the energy $\delta\mathcal{W}_{\mathrm{el}}$ with respect to a variation of the configuration $\delta\boldsymbol{s}$ is shown to be [47, 48, 13]:

$$\delta\mathcal{W}_{\mathrm{el}} = \int_{\Omega_1 \cup \Omega_2} \boldsymbol{\tau} : \hat{\nabla}\delta\boldsymbol{s} \,\mathrm{d}\Omega + \int_{\gamma} t_\gamma \,(\mathrm{div}_\tau\, \delta\boldsymbol{s}) \,\mathrm{d}\gamma, \tag{42}$$

where $\hat{\nabla}$ and div_τ respectively denote spatial symmetric gradient and surface divergence operators, and the following positions are introduced:

$$\boldsymbol{\tau} = \varepsilon \left[\boldsymbol{e} \otimes \boldsymbol{e} - \frac{1}{2} |\boldsymbol{e}|^2 \boldsymbol{I} \right], \quad t_\gamma = -\frac{1}{2} C\, [\![\varphi]\!]^2 . \tag{43}$$

Specifically, $\boldsymbol{\tau}$ is the Maxwell stress tensor, whereas t_γ is an hydrostatic membrane stress acting on the interface γ and dual to local area variations. Because of the constraint which locally prevents surface area modifications of the biological membrane, accounted for in Section 2.2.1, the hydrostatic membrane stress t_γ does not induce any deformation and can be neglected. Upon integrating by parts the Maxwell stress tensor contribution in equation (42), the electric field energy variation can be recast as:

$$\delta\mathcal{W}_{\mathrm{el}} = \int_{\Omega_1 \cup \Omega_2} -\boldsymbol{f} \cdot \delta\boldsymbol{s} \,\mathrm{d}\Omega + \int_{\gamma} -\boldsymbol{f}_\gamma \cdot \delta\boldsymbol{s} \,\mathrm{d}\gamma, \tag{44}$$

in which the volume and surface densities of the induced forces are respectively given by:

$$\boldsymbol{f} = \mathrm{div}\, \boldsymbol{\tau}, \quad \boldsymbol{f}_\gamma = [\![\boldsymbol{\tau}\boldsymbol{n}]\!] . \tag{45}$$

An explicit computation shows that, for vanishing free charges, the volume density is [36]:

$$\boldsymbol{f} = -\frac{1}{2}\, |\boldsymbol{e}|^2\, \nabla\varepsilon, \tag{46}$$

and indeed vanishes within homogeneous regions. Accordingly, the mechanical loads induced by the electric field to be considered in the solution of the mechanical problem boil down to the surface force density over the biological membrane $\boldsymbol{f}_\gamma$, as given in equation $(45)_2$.

As in the following developments high-frequency time-harmonic fields are considered, the Maxwell stress tensor $\boldsymbol{\tau}$ can be replaced by its time-averaged counterpart $\langle\boldsymbol{\tau}\rangle$. From the discussion in [49, 50], the latter can be expressed in terms of the electric field phasor $\boldsymbol{E}$ by:

$$\langle\boldsymbol{\tau}\rangle = \frac{1}{4}\, \varepsilon \left[\left(\boldsymbol{E} \otimes \overline{\boldsymbol{E}} + \overline{\boldsymbol{E}} \otimes \boldsymbol{E} \right) - |\boldsymbol{E}|^2 \boldsymbol{I} \right] . \tag{47}$$

3.3. Isogeometric discretization

An IGA formulation of the electrical problem (39) is considered. In particular, a multi-patch conforming discretization is adopted to describe the problem domain, which is composed of the intracellular space region Ω_1, the suspending fluid region Ω_2, the biological membrane γ and the electroded regions $\partial\Omega_{e_i}$. Over each patch, the geometry and the solution are approximated by:

$$\boldsymbol{x} = R_I\,\hat{\boldsymbol{x}}_I, \quad \Phi = R_I\,\hat{\Phi}_I, \tag{48}$$

where R_I is the basis function associated to the control point I, $\hat{\boldsymbol{x}}_I$ denotes the control point coordinates and $\hat{\Phi}_I$ denotes the control point electric potential phasor. Standard derivations, not discussed here, yield the problem stiffness matrix and the force vector (for instance, see [51]). From the solution of the corresponding linear system of equilibrium equations, the approximation of the electric potential phasor Φ is derived.

For the computation of the surface force density over the biological membrane $\boldsymbol{f}_\gamma$, the electric field phasor $\boldsymbol{E}$ is required on both sides of the interface. Conveniently, the following decomposition is considered:

$$\boldsymbol{E} = \boldsymbol{E}_\tau + E_{\boldsymbol{n}}\boldsymbol{n}, \tag{49}$$

in which $\boldsymbol{E}_\tau$ is the projection onto the interface tangent plane and $E_{\boldsymbol{n}}$ is the relevant normal component. According to equation (40), the surface projection $\boldsymbol{E}_\tau$ is computed as the surface gradient of the electric potential phasor Φ over the interface γ. Adopting the notation of Section 2 and exploiting the solution approximation $(48)_2$, it follows that:

$$\boldsymbol{E}_\tau = \nabla_\tau\,\Phi = R_{I,\alpha}\,\boldsymbol{g}^\alpha\,\hat{\Phi}_I, \tag{50}$$

where ∇_τ denotes the spatial surface gradient operator. An analogous derivation can be performed to derive the normal component $E_{\boldsymbol{n}}$. However, instead of resorting to the gradient of a discretized quantity, that would yield less accurate results, the interface admittance behavior $(36)_2$ can be exploited and it straightforwardly turns out that:

$$E_{\boldsymbol{n}} = -\frac{Y}{\sigma^*}\,[\![\varphi]\!]\,. \tag{51}$$

It is noted that neither the surface projection $\boldsymbol{E}_\tau$ nor the normal component $E_{\boldsymbol{n}}$ of the electric field phasor $\boldsymbol{E}$ is continuous across the interface γ. Indeed, relevant values of the control point electric potential phasor $\hat{\Phi}_I$ and of the complex conductivity σ^* are respectively considered in equations (50) and (51). Finally, equation (47) gives the time-averaged Maxwell stress tensor, whence the surface force density over the biological membrane follows from equation $(45)_2$.

4. Electro-mechanical coupling

In this section, the numerical procedure adopted for investigating the electro-deformation of a RBC, immersed in a suspending fluid and subjected to an applied electric field, is discussed. Specifically, the electro-mechanical strong coupling is addressed by resorting

to a staggered fixed-point iteration procedure. This approach allows to solve mechanical and electrical problems sequentially, relying on the two solvers respectively developed in Sections 2 and 3.

A loading history conducted under electrical potential control is considered. Let $n = 0, 1, \ldots$ denote the last converged loading step and let γ^n denote the corresponding RBC current shell surface, with $\gamma^0 = \Gamma$. A prescribed electrode potential $\varphi_{\mathrm{e}_i}^{n+1}$ is assumed to be applied on the i-th electrode at the loading step $n+1$. Furthermore, let $j = 0, 1, \ldots$ denote the last fixed-point iteration. The electrical problem (39) is solved assuming the RBC in the configuration $\gamma^{n+1,j}$, with $\gamma^{n+1,0} = \gamma^n$. Accordingly, the forces induced by the electric field $\boldsymbol{f}_\gamma^{n+1,j}$ acting on the RBC biological membrane can be computed from equation $(45)_2$, whence the control point external forces $\boldsymbol{q}_{\mathrm{ext}}^{n+1,j}$ follow by equation $(34)_2$. Correspondingly, the solution of the mechanical problem (27) yields an updated RBC current shell surface $\gamma^{n+1,j+1}$. The fixed-point iteration convergence is achieved when a global measure of the distance between $\gamma^{n+1,j+1}$ and $\gamma^{n+1,j}$, i.e. the distance of the corresponding control points, is lower than a given relative tolerance. The present procedure is summarized in Algorithm 1.

In order to facilitate the convergence of the numerical procedure, an adaptive substepping scheme, that automatically reduces the loading step whenever convergence is not achieved within a reasonable number of iterations, is also implemented. Moreover, the RBC current surface resulting from the last fixed point iteration, i.e. $\gamma^{n+1,j}$, is assumed as initial guess of Newton's method.

Algorithm 1: Fixed point iteration scheme for electro-mechanical coupling.

```
/* Initialization                                                          */
input i-th electrode potential φ_{e_i}^{n+1} at next loading step;
initialize j = 0;
initialize γ^{n+1,0} = γ^n;
initialize converged = false;
while ∼converged do
    /* Solve electrical problem for RBC current surface γ^{n+1,j}          */
    compute electric potential phasor Φ^{n+1,j} (equation (39));
    compute forces induced by the electric field f_γ^{n+1,j} (equations (49), (47), (45));
    /* Solve mechanical problem for current electric forces f_γ^{n+1,j}    */
    compute updated RBC current surface γ^{n+1,j+1} (equation (27));
    /* Convergence check                                                   */
    if ‖γ^{n+1,j+1} − γ^{n+1,j}‖ / ‖γ^{n+1,j}‖ > Tol then
        j + 1 ← j;
    else
        set converged = true;
    end if
end while
```

Table 1: Numerical parameters of the RBC geometric model [52].

$R\,[\mu\mathrm{m}]$	c_0	c_1	c_2
3.91	0.207161	2.002558	−1.122762

Table 2: Sets of constitutive parameters of the RBC mechanical model. Here $\beta = (k_\mathrm{B}T)^{-1}$, with k_B as the Boltzmann constant.

	$L_\mathrm{max}\,[\mathrm{nm}]$	$L_0\,[\mathrm{nm}]$	$p\,[\mathrm{nm}]$	q	$T\,[\mathrm{K}]$	βk_c	$k_\mathrm{g}/k_\mathrm{c}$	$\beta A_\mathrm{tp} k_\mathrm{s}$	$\beta V k_\mathrm{v}$
set 1 [15, 53]	166.1	75.5	18.7	1	296	48.9	−4/3	263.3	1.34×10^8
set 2 [34, 16]	238	75	7.5	1	296	48.9	−4/3	263.3	1.34×10^8
set 3 [16]	238	87	8.5	1	296	48.9	−4/3	263.3	1.34×10^8
set 4 [16]	238	91	9.5	1	296	48.9	−4/3	263.3	1.34×10^8

5. Numerical simulations

In this section, numerical simulations are reported for assessing accuracy, robustness and effectiveness of the proposed isogeometric formulation. First, a purely mechanical application, dealing with the large deformation of a RBC by optical tweezers is presented. The comparison with experimental results available in the literature [34] is used for validating the mechanical problem solution (Section 2). Then, the simulation of a RBC electro-deformation experiment, also relying on the electrical problem solution (Section 3) and the proposed electro-mechanical coupling scheme (Section 4), is discussed.

For both simulations, the RBC geometric model is obtained by revolution of the following meridional section [52]:

$$f(r) = \frac{R}{2}\sqrt{1-\left(\frac{r}{R}\right)^2}\left[c_0 + c_1\left(\frac{r}{R}\right)^2 + c_2\left(\frac{r}{R}\right)^4\right], \quad r \in [0, R]\,, \tag{52}$$

where the axial radius R and the shape coefficients c_0, c_1, c_2 are reported in Table 1. On such a basis, a polar NURBS surface is generated (a strategy for achieving optimal global convergence rates in a polar spline framework is discussed in [54]). Several sets of numerical parameters characterizing the RBC mechanical constitutive law (Section 2.2) are reported in Table 2. Details on their determination from experimental results are discussed in [11, 53, 15, 34].

All numerical experiments have been performed by means of an in-house MATLAB® code, and the computations have been done on a single machine with an Intel® Xeon® CPU processor E5-2660 v3 @ 2.60 GHz and 128 GB RAM.

5.1. RBC large deformation by optical tweezers

Among the experimental techniques explored for single-cell mechanical characterization, the deformation by optical tweezers has proved to be a powerful tool for studying the cell

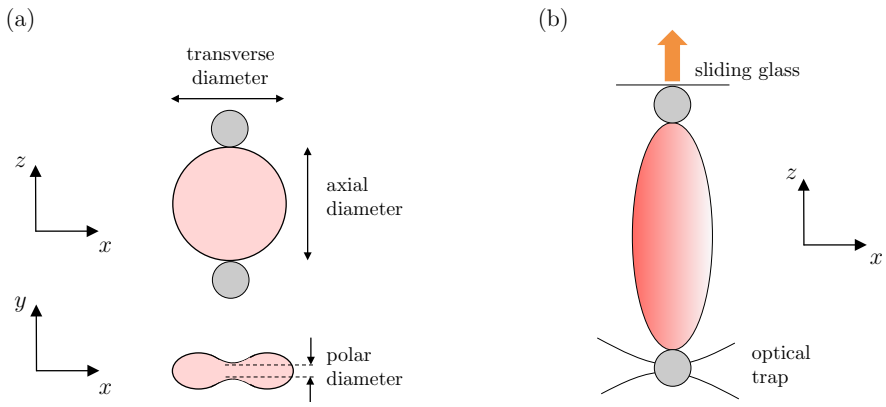

Figure 3: RBC large deformation by optical tweezers: (a) schematic representation of axial, transverse and polar diameters and (b) sketch of the experimental setup, assuming one bead to be optically trapped and the other one to be anchored to the surface of a moving glass slide, reprinted with permission from [13].

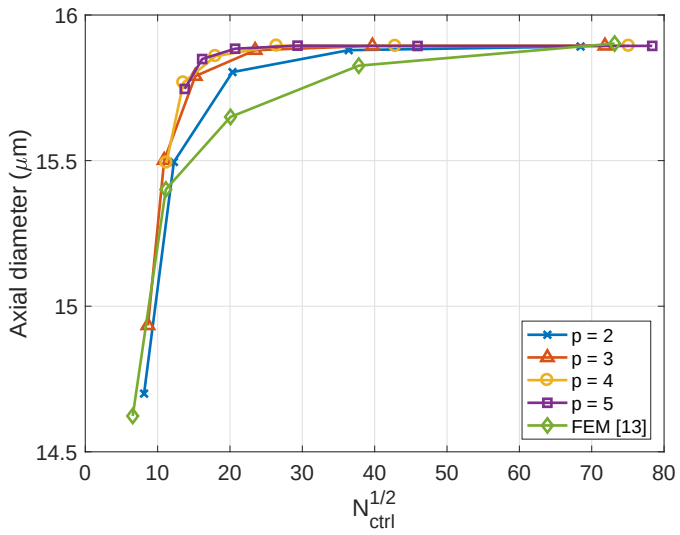

Figure 4: RBC large deformation by optical tweezers: h- and p- convergence analysis (k-refinement) in terms of deformed axial diameter at the end of the loading history versus square root number of control points. Results relevant to the FEM formulation in [13] are reported for comparison, with N_{ctrl} to be intended as the number of nodes.

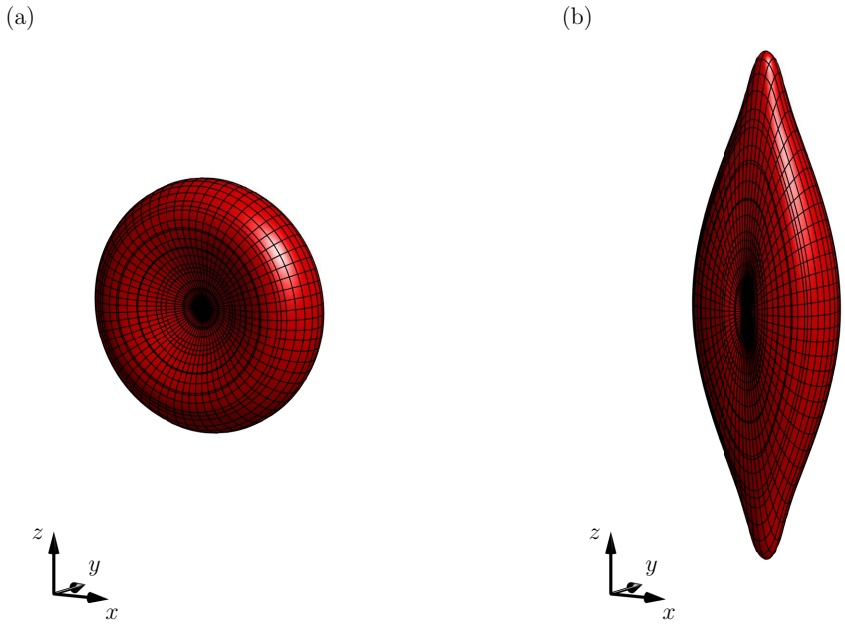

Figure 5: RBC large deformation by optical tweezers: (a) reference configuration and (b) deformed configuration under maximum applied load. A discretization with $N_{\text{ctrl}}^{1/2} \approx 24$ and $p = 3$.

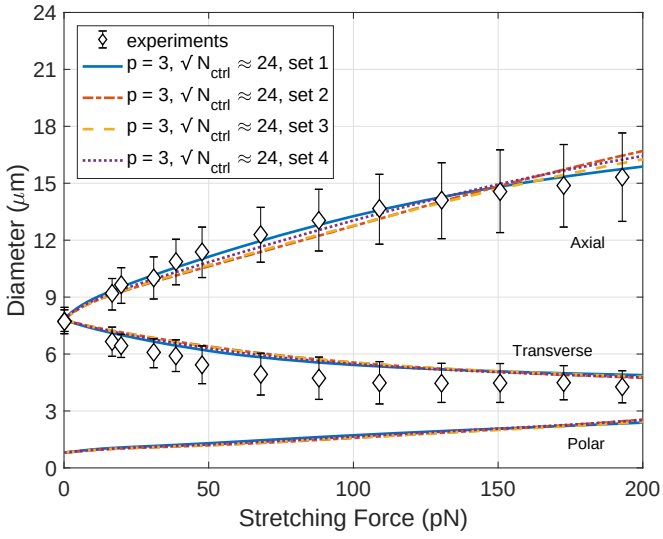

Figure 6: RBC large deformation by optical tweezers: axial, transverse and polar diameters versus stretching force for the sets of constitutive parameters in Table 2. Numerical results are compared with the experimental data reported in [12] (not including the polar diameter).

response under a variety of well-controlled stress states [12]. The experimental procedure, sketched in Figure 3, requires to attach two silica microbeads to the RBC at diametrically opposite points. While one microbead is fixed to the surface of a glass slide, the other one is optically trapped by means of a highly focused laser beam. As the trapped bead remains stationary, stretching forces can be applied in the RBC axial direction by moving the glass slide. Even if early studies primarily concerned small elastic deformation at low applied forces, the possibility of inducing large elastic deformation in RBCs was investigated in [10, 55, 56, 12]. In particular, considering a stretching force increasing up to a value of $193 \pm 20\,\mathrm{pN}$, overall axial stretches (i.e. relative changes in the axial diameter between deformed and undeformed configurations) in the order of 100% were recorded. Here, numerical simulations of the RBC large deformation by optical tweezers are performed by means of the proposed isogeometric formulation.

The stretching force imposed by the silica microbeads is modeled as a uniformly distributed force on a circular contact area of diameter $D = 1.1\,\mu\mathrm{m}$. The force resultant is linearly increased up to a maximum value $F_{\max} = 200\,\mathrm{pN}$ in $N_{\mathrm{s}} = 16$ loading steps. Constitutive parameters of set 1 in Table 2 are considered for the RBC mechanical constitutive law. Because of problem symmetry, only one-eight of the RBC is modeled and appropriate boundary conditions are applied on the symmetry planes (rotational constraints are imposed by assuming coincident displacements for the control points on the symmetry planes and their adjacent ones). In order to explore h- and p-convergence properties of the present formulation, the problem is solved adopting discretizations corresponding to different levels of mesh refinement and different NURBS degrees. Specifically, each mesh is characterized by the square root of the total number of its control points N_{ctrl}, approximately ranging from 7 to 80, and its polynomial degree p, ranging from 2 to 5.

In Figure 4 the results of h- and p-convergence analysis (with refinement conducted by degree elevation followed by knot insertion, i.e. with k-refinement) are reported in terms of the deformed axial diameter at the end of the loading history. The expected convergence is achieved (the solution at convergence of the k-refinement analysis is $15.894\,\mu\mathrm{m}$), with increasing velocity for increasing polynomial degree. For comparison, results relevant to h-convergence analysis of the rotation-free finite element shell proposed in [13] are also reported, by interpreting N_{ctrl} as the number of nodes. As expected, a much faster convergence of the present IGA formulation can be observed with respect to the FEM approximation.

Considering a discretization with $N_{\mathrm{ctrl}}^{1/2} \approx 24$ and $p = 3$, the reference and deformed configuration under maximum load level are respectively depicted in Figure 5(a) and Figure 5(b). For the same discretization, in Figure 6 the behavior of axial, transverse and polar diameters is shown as a function of the stretching force. For investigating how the results depend on the RBC constitutive parameters, curves corresponding to the parameter sets in Table 2 are shown. In addition, experimental results from [34] are reported for comparison. Excellent agreement is observed in the axial diameter prediction, whereas slight differences can be noticed in the transverse diameter prediction (experimental results relevant to polar diameter are not available). As noted in [15], that is probably due to an underestimation in the experimental results, because optical measurements are performed from a single observation angle only and the RBC can rotate during the test. Nevertheless, numerical results

Table 3: RBC electro-deformation: constitutive parameters of the electrical model adopted for RBC [57], electrodes [57], and suspending fluid [9].

σ_1 [S/m]	ε_1	σ_2 [S/m]	ε_2	C [mF/m^2]	C_e [mF/m^2]
0.5	60	0.05	80	10	144

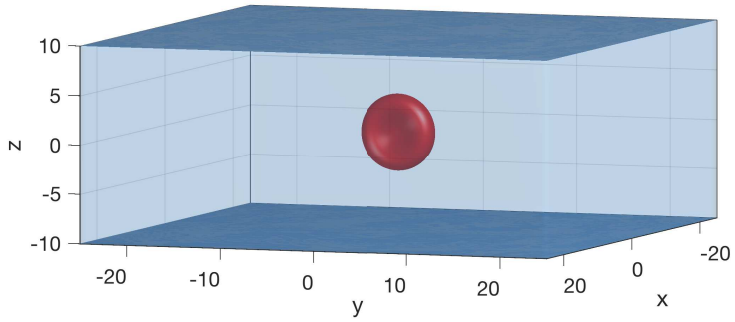

Figure 7: RBC electro-deformation: an erythrocyte is immersed in a suspending fluid and subjected to an applied electric field. Multipatch conforming discretization is adopted to describe the problem domain, composed of the biological membrane and of the intracellular space region (red), of the suspending fluid region (light blue) and of the electroded regions (dark blue).

remain within the experimental error bars. It is remarked that the RBC biconcave shape progressively turns into a more rounded shape under the simultaneous effect of the stretching forces and of the enclosed-volume conservation constraint. Moreover, a hardening behavior is exhibited by the RBC structure during the deformation process, as it is expected by the nonlinear constitutive properties of the spectrin network.

5.2. RBC electro-deformation

With the aim of performing an *in silico* RBC electro-deformation experiment, the setup depicted in Figure 7 is considered. Specifically, a RBC is immersed in a suspending fluid and placed between two facing electrodes, of dimensions $50\,\mu\mathrm{m} \times 50\,\mu\mathrm{m}$ and at $20\,\mu\mathrm{m}$ distance from each other. On the top electrode a voltage at frequency $f = 500\,\mathrm{kHz}$ and increasing up to a maximum value $V_\mathrm{max} = 2.0\,\mathrm{V}$ is applied in $N_\mathrm{s} = 16$ loading steps, whereas the bottom

Table 4: RBC electro-deformation: overall CPU time needed for the electro-mechanical coupling. A discretization with $N_\mathrm{ctrl}^{1/2} \approx 24$ [resp., $N_\mathrm{ctrl}^{1/3} \approx 28$] for the mechanical [resp., electrical] problem and $p = 3$ is assumed. Data relevant to the converged mesh for the FEM formulation in [13] are reported for comparison.

	Mechanical problem		Electrical problem		
Discretization	$N_\mathrm{ctrl}^{1/2}$	N_dof	$N_\mathrm{ctrl}^{1/3}$	N_dof	CPU time
NURBS, $p = 3$	24	1,740	28	22,040	4,959 s
FEM [13]	49	7,032	54	159,329	48,075 s

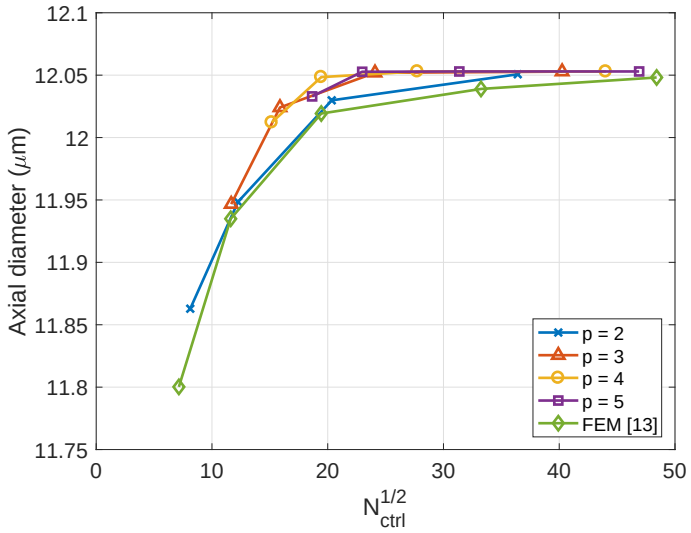

Figure 8: RBC electro-deformation: h- and p- convergence analysis (k-refinement) in terms of deformed axial diameter under the maximum applied electric potential versus square root number of control points of the mechanical problem discretization. Results relevant to the FEM formulation in [13] are reported for comparison, with N_{ctrl} to be intended as the number of nodes of the mechanical problem discretization.

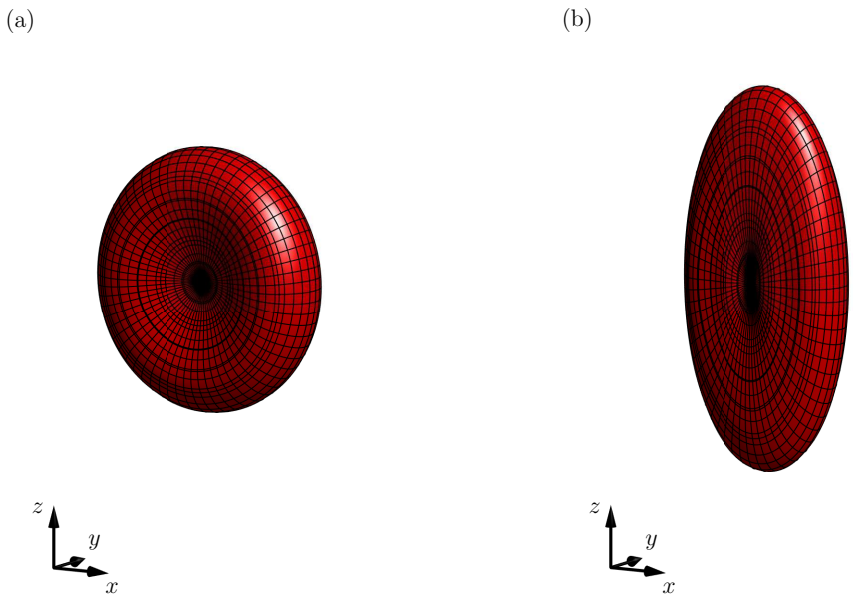

Figure 9: RBC electro-deformation: (a) reference configuration and (b) deformed configuration under the maximum applied electric potential. A discretization with $N_{\text{ctrl}}^{1/2} \approx 24$ [resp., $N_{\text{ctrl}}^{1/3} \approx 28$] for the mechanical [resp., electrical] problem and $p = 3$ is assumed.

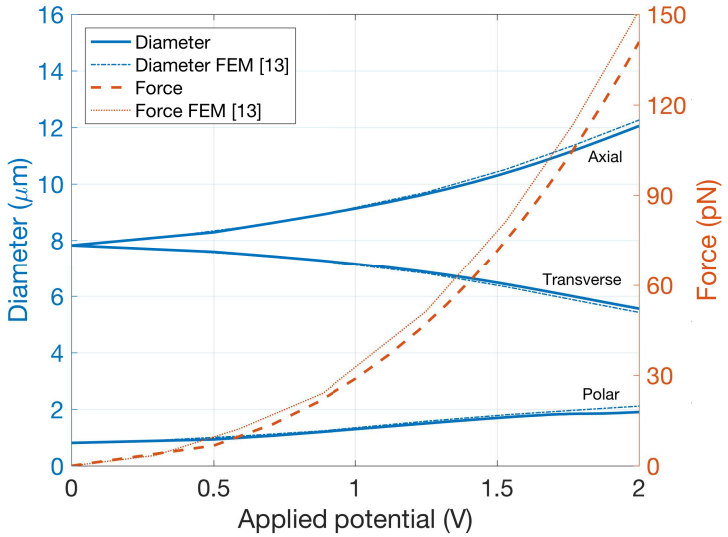

Figure 10: RBC electro-deformation: axial, transverse, polar diameters and half-cell resultant force in z-direction versus applied electric potential. Results relevant to the converged mesh for the FEM formulation in [13] are reported for comparison.

electrode is grounded.

Set 1 of constitutive parameters in Table 2 is considered for the RBC mechanical constitutive law. The electrical constitutive parameters characterizing the biological membrane, the intracellular space, the suspending fluid and the electrodes are reported in Table 3, adopting the notation introduced in Section 3. As typical in electro-deformation experiments, a poorly conductive suspending fluid is considered, in such a way that positive dielectrophoretic forces are generated [9]. Moreover, in the present radio-frequency range, the biological membrane [resp. electrode] conductance per unit area G [resp. G_{e}] is assumed to be vanishing, since it is negligible compared to ωC [resp. ωC_{e}]. Accordingly, the biological membrane and the electrode behave as capacitors.

Due to problem symmetry, only one-eight of the computational domain is modeled. In particular, four conforming patches are adopted for describing the intracellular space and the suspending fluid regions (volumetric patches), the biological membrane and the top electrode (surface patches). For investigating h- and p-convergence properties of the present formulation, discretizations characterized by different levels of mesh refinement and different NURBS degrees are considered. In particular, the meshes adopted for the biological membrane [resp., for the intracellular space and the suspending fluid regions] involve a number of control points N_{ctrl} such that its square [resp., cubic] root approximately ranges from 7 to 50 [resp., from 6 to 55], with polynomial degree p ranging from 2 to 5. The relative tolerance assumed for detecting the convergence of the staggered fixed-point iteration scheme is set to 0.001.

Figure 8 shows the results of h- and p-convergence analysis (k-refinement) in terms of the deformed axial diameter under the maximum applied electric potential. The convergence at

the solution 12.05 μm is reached with increasing velocity for increasing polynomial degree. Results relevant to h-convergence analysis of the rotation-free finite element shell proposed in [13] are also reported. Similarly to the purely mechanical application discussed in the previous section, the present IGA formulation exhibits faster convergence than the FEM alternative.

Considering a discretization with $N_{\text{ctrl}}^{1/2} \approx 24$ [resp., $N_{\text{ctrl}}^{1/3} \approx 28$] for the mechanical [resp., electrical] problem and $p = 3$, which is already at convergence, the RBC reference and deformed configuration under maximum applied voltage are shown in Figure 9(a) and Figure 9(b), respectively. In Figure 10, axial, transverse and polar diameters, along with the resultant force along z-direction over half cell, are reported versus the applied electric potential. Under the maximum applied electric potential, a resultant force of 140.8 pN is computed and the corresponding RBC deformed configuration exhibits axial diameter of 12.05 μm, transverse diameter of 5.56 μm and polar diameter of 1.90 μm. The number of fixed-point iterations in each loading step, needed to reach convergence in the electro-mechanical coupling scheme, ranges between 2 and 5, with average value of 3.1. For comparison, the solution obtained by the converged mesh for the FEM formulation in [13], characterized by a number of nodes $N_{\text{ctrl}}^{1/2} \approx 49$ [resp., $N_{\text{ctrl}}^{1/3} \approx 54$] for the mechanical [resp., electrical] problem, is also reported. Slight differences, due to the more accurate geometric model provided by IGA framework compared to FEM, can be observed. In Table 4 a comparison on the overall CPU time needed to perform the electro-mechanical coupling is reported between such IGA and FEM discretizations. Superior performances of the present IGA formulation can be highlighted.

As suggested in [9], electro-deformation experiments can be used in conjunction with microfluidic systems as quantitative, high-throughput characterization techniques of the biomechanical properties of a large number of single cells. Accordingly, label-free biomarkers might be derived for distinguishing healthy from pathological states of human cells. In this context, the present isogeometric analysis formulation, thanks to its robustness, accuracy and effectiveness, represents a valuable tool for an inverse analysis approach aiming at such microstructural biomechanical properties characterization. In addition, it might be exploited for assisting the design of optimal electro-deformation systems, in terms of geometry, medium properties and voltage frequency.

6. Conclusions

An isogeometric formulation for modeling the electro-deformation of a red blood cell has been presented. The mechanical description of the RBC behavior has been based on the understanding that its structure is composed of a biological membrane enclosing a nearly-incompressible fluid. A surface shell model, similar to the Kirchhoff–Love model but not involving the shell thickness, has been proposed for capturing the RBC kinematics. A homogenized microstructurally-based constitutive law, based on the Cauchy–Born rule, has been adopted for the membrane behavior of the biological membrane, in order to accurately account for all its constituents, yet enjoying the computational efficiency of a continuum approach. The Helfrich model has been assumed for the bending behavior of the biological

membrane. Finally, an enclosed-volume conservation constraint has been enforced at structural level to model the volumetric behavior arising from the nearly-incompressible fluid inside the biomembrane. For the electrical problem, dealing with a RBC immersed in a suspending fluid and subjected to an applied electric field, conforming patches have been employed for describing the biological membrane, the intracellular space and the suspending fluid regions. An accurate computation of the mechanical forces induced by the electric field acting upon the RBC has been performed resorting to the Maxwell stress tensor formulation. A staggered fixed-point iteration scheme has been presented for performing the electro-mechanical strong coupling, in such a way that electrical and mechanical problems can be solved in an uncoupled way by means of respective reliable solvers. Specifically, the two solvers communicate through the biological membrane current configuration (computed by the mechanical solver) and the mechanical forces induced by the electric field (computed by the electrical solver). The convergence is achieved when the current configuration is in equilibrium under the relevant forces. Numerical simulations reproducing RBC large deformation by optical tweezers and RBC electro-deformation have been performed. The comparison with experimental evidences and reference solutions proves accuracy, robustness and effectiveness of the proposed isogeometric formulation. In addition, a reduction in computational cost with respect to a typical finite element discretization available in the literature, due to the ability of the isogeometric formulation to attain convergence for a lower number of degrees of freedom, is highlighted.

Appendix A. Mechanical problem linearization

The structural equilibrium conditions for the mechanical evolution of a RBC have been derived within IGA framework in equation (33). For adopting Newton's method of solution, their linearization with respect to the control point displacements $\hat{\boldsymbol{u}}$ is needed.

With regard to the control point internal forces $\boldsymbol{q}_{\text{int}}$, the structural consistent stiffness matrix $\boldsymbol{K}_{\text{int}}$ is introduced by:

$$\begin{aligned}\boldsymbol{K}_{\text{int}}\,\Delta\hat{\boldsymbol{u}}\cdot\delta\hat{\boldsymbol{u}} &= \Delta\boldsymbol{q}_{\text{int}}\cdot\delta\hat{\boldsymbol{u}} = \Delta\delta\mathcal{W}_{\text{int}}\\ &= \int_{\Gamma}\left(\Delta\boldsymbol{n}:\delta\boldsymbol{\varepsilon}+\boldsymbol{n}:\Delta\delta\boldsymbol{\varepsilon}\right)\,\mathrm{d}\Gamma\\ &+ \int_{\Gamma}\left\{\left(\Delta\boldsymbol{m}:\delta\boldsymbol{\chi}+\boldsymbol{m}:\Delta\delta\boldsymbol{\chi}\right)\Lambda+\boldsymbol{m}:\delta\boldsymbol{\chi}\,\Delta\Lambda+\boldsymbol{m}:\Delta\boldsymbol{\chi}\,\delta\Lambda+w_{\text{b}}\,\Delta\delta\Lambda\right\}\,\mathrm{d}\Gamma\\ &+ \left(\Delta p\,\delta v+p\,\Delta\delta v\right),\end{aligned} \tag{A.1}$$

where Δ denotes the linearization operator and the linearization of the shell membrane forces $\boldsymbol{n}$, of the shell bending forces $\boldsymbol{m}$ and of the shell inner pressure p, respectively following from equations (21), (23) and (25), reads:

$$\Delta\boldsymbol{n}=\frac{\partial^2 w_{\text{m}}}{\partial\boldsymbol{\varepsilon}^2}\,\Delta\boldsymbol{\varepsilon},\quad \Delta\boldsymbol{m}=\frac{\partial^2 w_{\text{b}}}{\partial\boldsymbol{\chi}^2}\,\Delta\boldsymbol{\chi},\quad \Delta p=\frac{\partial^2\mathcal{W}_{\text{v}}}{\partial v^2}\,\Delta v. \tag{A.2}$$

Analogously to the derivation of the weak equilibrium formulation, the linearization of the variations of the change of metric tensor $\Delta\delta\boldsymbol{\varepsilon}$, of the change of curvature tensor $\Delta\delta\boldsymbol{\chi}$ and of the change of enclosed volume $\Delta\delta v$ is required. To this end, first the linearization of the variation of the current surface configuration is performed. From equations (32) it is observed that:

$$\Delta\delta\boldsymbol{x} = \boldsymbol{0}, \quad \Delta\delta\boldsymbol{g}_\alpha = \boldsymbol{0}, \tag{A.3}$$

whereas from equation $(9)_3$:

$$\Delta\delta\boldsymbol{g}_3 = -\left(\Delta\boldsymbol{g}_3 \otimes \boldsymbol{g}_3 + \boldsymbol{g}_3 \otimes \Delta\boldsymbol{g}_3\right)\frac{\delta\tilde{\boldsymbol{g}}_3}{a} + \left(\boldsymbol{I} - \boldsymbol{g}_3 \otimes \boldsymbol{g}_3\right)\left(\frac{\Delta\delta\tilde{\boldsymbol{g}}_3}{a} - \frac{\delta\tilde{\boldsymbol{g}}_3\Delta a}{a^2}\right), \tag{A.4}$$

in which from equation (10):

$$\Delta\delta\tilde{\boldsymbol{g}}_3 = \delta\boldsymbol{g}_1 \times \Delta\boldsymbol{g}_2 + \Delta\boldsymbol{g}_1 \times \delta\boldsymbol{g}_2, \quad \Delta\delta a = \Delta\boldsymbol{g}_3 \cdot \delta\tilde{\boldsymbol{g}}_3 + \boldsymbol{g}_3 \cdot \Delta\delta\tilde{\boldsymbol{g}}_3. \tag{A.5}$$

Next, from equations (11) and (12):

$$\Delta\delta\boldsymbol{\varepsilon} = \frac{1}{2}\left(\delta\boldsymbol{g}_\alpha \cdot \Delta\boldsymbol{g}_\beta + \Delta\boldsymbol{g}_\alpha \cdot \delta\boldsymbol{g}_\beta\right)\boldsymbol{G}^\alpha \otimes \boldsymbol{G}^\beta, \tag{A.6}$$

$$\Delta\delta\boldsymbol{\chi} = -\left(\delta\boldsymbol{g}_{\alpha,\beta} \cdot \Delta\boldsymbol{g}_3 + \Delta\boldsymbol{g}_{\alpha,\beta} \cdot \delta\boldsymbol{g}_3 + \boldsymbol{g}_{\alpha,\beta} \cdot \Delta\delta\boldsymbol{g}_3\right)\boldsymbol{G}^\alpha \otimes \boldsymbol{G}^\beta, \tag{A.7}$$

and from equation (13):

$$\Delta\delta v = \frac{1}{3}\int_\Gamma [\delta\boldsymbol{x} \cdot (\Delta\boldsymbol{g}_3\,\Lambda + \boldsymbol{g}_3\,\Delta\Lambda) + \Delta\boldsymbol{x} \cdot (\delta\boldsymbol{g}_3\,\Lambda + \boldsymbol{g}_3\,\delta\Lambda) + \boldsymbol{x} \cdot (\Delta\delta\boldsymbol{g}_3\,\Lambda + \delta\boldsymbol{g}_3\,\Delta\Lambda + \Delta\boldsymbol{g}_3\,\delta\Lambda + \boldsymbol{g}_3\,\Delta\delta\Lambda)]\,\mathrm{d}\Gamma, \tag{A.8}$$

in which from equation (14):

$$\Delta\delta\Lambda = \Delta\delta a/A. \tag{A.9}$$

A similar treament for the control point external forces $\boldsymbol{q}_{\text{ext}}$ leads to the introduction of an external stiffness matrix $\boldsymbol{K}_{\text{ext}}$. However, in the present work, the coupling between electrical and mechanical modules is treated through the fixed-point iteration scheme discussed in Section 4 and such stiffness contribution needs not be accounted for. On the other hand, its computation would be necessary for a monolithic solution strategy of the coupled problem adopting Newton's method.

Acknowledgements

This work was supported by he Scientific Independence of Young Researchers Programme (SIR 2014) under Grant RBSI14TX20-MUSIC "Multidimensional Single-Cell Microfluidic Impedance Cytometry".

References

[1] D. Di Carlo, A mechanical biomarker of cell state in medicine, J. Lab. Autom. 17 (1) (2012) 32–42. doi:10.1177/2211068211431630.

[2] D. H. Kim, P. K. Wong, J. Park, A. Levchenko, Y. Sun, Microengineered platforms for cell mechanobiology, Annu. Rev. Biomed. Eng. 11 (2009) 203–233. doi:10.1146/annurev-bioeng-061008-124915.

[3] M. L. Rodriguez, P. J. McGarry, N. J. Sniadecki, Review on cell mechanics: Experimental and modeling approaches, Appl. Mech. Rev. 65 (6) (2013) 060801–060801–41. doi:10.1115/1.4025355.

[4] I. L. Ahmad, M. R. Ahmad, Trends in characterizing single cell's stiffness properties, Micro. Nano. Syst. Lett. 2 (8). doi:10.1186/s40486-014-0008-5.

[5] P. K. Wong, W. Tan, C. M. Ho, Cell relaxation after electrodeformation: effect of latrunculin a on cytoskeletal actin, J. Biomech. 38 (3) (2005) 529–535. doi:10.1016/j.jbiomech.2004.04.008.

[6] L. A. MacQueen, M. D. Buschmann, M. R. Wertheimer, Mechanical properties of mammalian cells in suspension measured by electro-deformation, J. Micromech. Microeng. 20 (2010) 065007. doi:10.1088/0960-1317/20/6/065007.

[7] J. Chen, M. Abdelgawad, L. Yu, N. Shakiba, W.-Y. Chien, Z. Lu, W. R. Geddie, M. A. S. Jewett, Y. Sun, Electrodeformation for single cell mechanical characterization, J. Micromech. Microeng. 21 (2011) 054012. doi:10.1088/0960-1317/21/5/054012.

[8] S. L. Leung, Y. Lu, D. Bluestein, M. J. Slepian, Dielectrophoresis-mediated electrodeformation as a means of determining individual platelet stiffness, Annu. Rev. Biomed. Eng. (2015) 1–11doi:10.1007/s10439-015-1383-7.

[9] E. Du, M. Dao, S. Suresh, Quantitative biomechanics of healthy and diseased human red blood cells using dielectrophoresis in a microfluidic system, Extr. Mech. Lett. 1 (2014) 35–41. doi:10.1016/j.eml.2014.11.006.

[10] M. Dao, C. T. Lim, S. Suresh, Mechanics of the human red blood cell deformed by optical tweezers, J. Mech. Phys. Solids 51 (11–12) (2003) 2259–2280. doi:10.1016/j.jmps.2003.09.019.

[11] D. E. Discher, D. H. Boal, S. K. Boey, Simulations of the erythrocyte cytoskeleton at large deformation. II. Micropipette aspiration, Biophys. J. 75 (3) (1998) 1584–1597. doi:10.1016/S0006-3495(98)74076-7.

[12] J. P. Mills, L. Qie, M. Dao, C. T. Lim, S. Suresh, Nonlinear elastic and viscoelastic deformation of the human red blood cell with optical tweezers, Mech. Chem. Biosyst. 1 (3) (2004) 169–80.

[13] N. A. Nodargi, P. Bisegna, F. Caselli, Effective computational modeling of erythrocyte electro–deformation, Meccanica 52 (3) (2016) 613–631. doi:10.1007/s11012-016-0424-0.

[14] I. V. Pivkin, G. E. Karniadakis, Accurate coarse-grained modeling of red blood cells, Phys. Rev. Lett. 101 (11) (2008) 118105. doi:10.1103/PhysRevLett.101.118105.

[15] D. A. Fedosov, B. Caswell, G. E. Karniadakis, A multiscale red blood cell model with accurate mechanics, rheology, and dynamics, Biophys. J. 98 (10) (2010) 2215–2225. doi:10.1016/j.bpj.2010.02.002.

[16] A. S. Ademiloye, L. W. Zhang, K. M. Liew, A multiscale framework for large deformation modeling of rbc membranes, Comput. Meth. Appl. Mech. Eng. 329 (2018) 144–167. doi:10.1016/j.cma.2017.10.004.

[17] A. S. Ademiloye, L. W. Zhang, K. M. Liew, Atomistic–continuum model for probing the biomechanical properties of human erythrocyte membrane under extreme conditions, Comput. Meth. Appl. Mech. Eng. 325 (2017) 22–36. doi:10.1016/j.cma.2017.06.033.

[18] L. W. Zhang, A. S. Ademiloye, K. M. Liew, A multiscale cauchy–born meshfree model for deformability of red blood cells parasitized by Plasmodium falciparum, J. Mech. Phys. Solids 101 (2017) 268–284. doi:10.1016/j.jmps.2017.01.009.

[19] A. Rosolen, C. Peco, M. Arroyo, An adaptive meshfree method for phase-field models of biomembranes. Part I: Approximation with maximum-entropy basis functions, J. Comput. Phys. 249 (2013) 303–319. doi:10.1016/j.jcp.2013.04.046.

[20] C. Peco, A. Rosolen, M. Arroyo, An adaptive meshfree method for phase-field models of biomembranes. Part II: A Lagrangian approach for membranes in viscous fluids, J. Comput. Phys. 249 (2013) 320–336. doi:10.1016/j.jcp.2013.04.038.

[21] L. Yang, J. C. Effler, B. L. Kutscher, S. E. Sullivan, D. N. Robinson, P. A. Iglesias, Modeling cellular

deformations using the level set formalism, BMC Syst. Biol. 2 (68) (2008) 1–16. doi:10.1186/1752-0509-2-68.
[22] A. Laadhari, P. Saramito, C. Misbah, An adaptive finite element method for the modeling of the equilibrium of red blood cells, Int J Numer Methods Eng 80 (2016) 397–428. doi:10.1002/fld.4086.
[23] T. J. R. Hughes, J. A. Cottrell, Y. Bazilevs, Isogeometric analysis: CAD, finite elements, NURBS, exact geometry and mesh refinement, Comput. Meth. Appl. Mech. Eng. 194 (2005) 4135–4195. doi:10.1016/j.cma.2004.10.008.
[24] J. Kiendl, K.-U. Bletzinger, J. Linhard, R. Wüchner, Isogeometric shell analysis with Kirchhoff–Love elements, Comput. Meth. Appl. Mech. Eng. 198 (2009) 3902–3914. doi:10.1016/j.cma.2009.08.013.
[25] J. Kiendl, M. C. Hsu, M. C. H. Wu, A. Reali, Isogeometric Kirchhoff–Love shell formulations for general hyperelastic materials, Comput. Meth. Appl. Mech. Eng. 291 (2015) 280–303. doi:10.1016/j.cma.2015.03.010.
[26] A. B. Tepole, H. Kabaria, K.-U. Bletzinger, E. Kuhl, Isogeometric Kirchhoff–Love shell formulations for biological membranes, Comput. Meth. Appl. Mech. Eng. 293 (2015) 328–347. doi:10.1016/j.cma.2015.05.006.
[27] Y. Bazilevs, V. M. Calo, Y. Zhang, T. J. R. Hughes, Isogeometric fluid–structure interaction analysis with applications to arterial blood flow, Comput. Mech. 38 (2006) 310–322. doi:10.1007/s00466-006-0084-3.
[28] Y. Bazilevs, V. M. Calo, T. J. R. Hughes, Y. Zhang, Isogeometric fluid-structure interaction: theory, algorithms, and computations, Comput. Mech. 43 (2008) 3–37. doi:10.1007/s00466-008-0315-x.
[29] E. B. Tadmor, G. S. Smith, N. Bernstein, E. Kaxiras, Mixed finite element and atomistic formulation for complex crystals, Phys. Rev. B 59 (1999) 235–245. doi:10.1103/PhysRevB.59.235.
[30] X. Wang, X. Guo, Z. Su, A quasi-continuum model for human erythrocyte membrane based on the higher order Cauchy–Born rule, Comput Meth Appl Mech Eng 268 (1) (2014) 284–298. doi:10.1016/j.cma.2013.08.020.
[31] A. S. Ademiloye, L. W. Zhang, K. M. Liew, Numerical computation of the elastic and mechanical properties of red blood cell membrane using the higher-order Cauchy–Born rule, Appl. Math. Comput. 268 (1) (2015) 334–353. doi:10.1016/j.amc.2015.06.071.
[32] M. Arroyo, T. Belytschko, Finite crystal elasticity of carbon nanotubes based on the exponential Cauchy–Born rule, Phys. Rev. B 69 (2004) 115415. doi:10.1103/PhysRevB.69.115415.
[33] H. S. Park, P. A. Klein, G. J. Wagner, A surface Cauchy–Born model for nanoscale materials, Int. J. Numer. Methods Eng. 68 (10) (2006) 1072–1095. doi:10.1002/nme.1754.
[34] J. Li, M. Dao, C. T. Lim, S. Suresh, Spectrin-level modeling of the cytoskeleton and optical tweezers stretching of the erythrocyte, Biophys. J. 88 (5) (2005) 3707–3719. doi:10.1529/biophysj.104.047332.
[35] W. Helfrich, Elastic properties of lipid bilayers: theory and possible experiments, Z. Naturforsch. C 28 (11) (1973) 693–703.
[36] J. A. Stratton, Electromagnetic Theory, McGraw-Hill, 1941.
[37] P. G. Ciarlet, An Introduction to Differential Geometry with Applications to Elasticity, Springer Netherlands, 2005. doi:10.1007/1-4020-4248-5.
[38] M. Bischoff, K.-U. Bletzinger, W. A. Wall, E. Ramm, Models and Finite Elements for Thin-Walled Structures, in: E. Stein, R. de Borst, T. J. R. Hughes (Eds.), Encyclopedia of Computational Mechanics, Vol. 2: Solids and Structures, John Wiley & Sons, Ltd., 2004, Ch. 3, pp. 1–25. doi:10.1002/0470091355.ecm026.
[39] D. E. Discher, D. H. Boal, S. K. Boey, Phase transitions and anisotropic responses of planar triangular nets under large deformation, Phys. Rev. E. 55 (4) (1997) 4762–4772. doi:10.1103/PhysRevE.55.4762.
[40] S. K. Boey, D. H. Boal, D. E. Discher, Simulations of the erythrocyte cytoskeleton at large deformation. I. Microscopic models, Biophys. J. 75 (3) (1998) 1573–1583. doi:10.1016/S0006-3495(98)74075-5.
[41] J. C. M. Lee, D. T. Wong, D. E. Discher, Direct measures of large, anisotropic strains in deformation of the erythrocyte cytoskeleton, Biophys. J. 77 (2) (1999) 853–864. doi:10.1016/S0006-3495(99)76937-7.
[42] J. F. Marko, E. D. Siggia, Stretching DNA, Macromolecules 28 (26) (1995) 8759–8770. doi:10.1021/ma00130a008.

[43] C. Bustamante, Z. Bryant, S. B. Smith, Ten years of tension: single-molecule DNA mechanics, Nature 421 (2003) 423–427. doi:10.1038/nature01405.
[44] L. Piegl, W. Tiller, The NURBS book, 2nd Edition, Springer-Verlag, New York, USA, 1997. doi:10.1007/978-3-642-97385-7.
[45] E. Somersalo, M. Cheney, D. Isaacson, Existence and uniqueness for electrode models for electric current computed tomography, SIAM J Appl Math 52 (1992) 1023–1040. doi:10.1137/0152060.
[46] L. D. Landau, E. M. Lifshitz, Electrodynamics of Continuous Media (Second Edition Revised and Enlarged), second edition revised and enlarged Edition, Vol. 8 of Course of Theoretical Physics, Pergamon, Amsterdam, 1984.
[47] A. Kirsch, The domain derivative and two applications in inverse scattering theory, Inverse Prob. 9 (1) (1999) 81–96. doi:10.1088/0266-5611/9/1/005.
[48] W. J. Yan, Y. C. Ma, The application of domain derivative for heat conduction with mixed condition in shape reconstruction, Appl. Math. Comput. 181 (2) (2006) 894–902. doi:10.1016/j.amc.2006.02.011.
[49] X. Wang, X. B. Wang, P. R. C. Gascoyne, General expressions for dielectrophoretic force and electrorotational torque derived using the Maxwell stress tensor method, J. Electrostat. 39 (4) (1997) 277–295. doi:10.1016/S0304-3886(97)00126-5.
[50] M. P. Vlahovska, R. S. Gracià, S. Aranda-Espinoza, R. Dimova, Electrohydrodynamic model of vesicle deformation in alternating electric fields, Biophys. J. 96 (12) (2009) 4789–4803. doi:10.1016/j.bpj.2009.03.054.
[51] J. A. Cottrell, T. J. R. Hughes, Y. Bazilevs, Isogeometric Analysis: Toward Integration of CAD and FEA, Wiley Publishing, Chichester, UK, 2009.
[52] E. Evans, Y. C. Fung, Improved measurements of erythrocyte geometry, Microvasc. Res. 4 (4) (1972) 335–47. doi:10.1016/0026-2862(72)90069-6.
[53] D. Fedosov, Multiscale modeling of blood flow and soft matter, Ph.D. thesis, Division of Applied Mathematics, Brown University, USA (2010).
[54] D. Toshniwal, H. Speleers, R. R. Hiemstra, T. J. R. Hughes, Multi-degree smooth polar splines: A framework for geometric modeling and isogeometric analysis, Comput Meth Appl Mech Eng 316 (1) (2017) 1005–1061. doi:10.1016/j.cma.2016.11.009.
[55] C. T. Lim, M. Dao, S. Suresh, C. H. Sow, K. T. Chew, Large deformation of living cells using laser traps, Acta Mat. 52 (7) (2004) 1837–1845. doi:10.1016/j.actamat.2004.05.016.
[56] C. T. Lim, M. Dao, S. Suresh, C. H. Sow, K. T. Chew, Corrigendum to "Large deformation of living cells using laser traps" [Acta Mat. 52(7) (2004) 1837–1845], Acta Mat. 52 (13) (2004) 4065–4066. doi:10.1016/j.actamat.2004.05.016.
[57] S. Gawad, K. Cheung, U. Seger, A. Bertsch, P. Renaud, Dielectric spectroscopy in a micromachined flow cytometer: theoretical and practical considerations, Lab. Chip. 4 (2004) 241–251. doi:10.1039/b313761a.